# Doping-engineering PdRu bimetallic nanoalloys with nitric oxide delivery for synergetic photodynamic therapy

*Chengchen Jia[a], Shiyu Zhang[a], Wubin Lv[a], Siyi Li[a], Yuxuan Zhao[a], Shuming Dong[*a], He Ding[*a,b], Ziaur Rehman[*c], and Piaoping Yang[*a]*

[a] *Key Laboratory of Superlight Materials and Surface Technology, Ministry of Education, College of Material Sciences and Chemical Engineering, Harbin Engineering University, Harbin, 150001, China*

[b] *Yangtze Delta Region Advanced Research Institute of Harbin Engineering University, Harbin Engineering University, Nantong, 226000, China*

[c] *Department of Chemistry, Quaid-i-Azam University, 45320, Islamabad, Pakistan*

**Table S1.** Comparison of key parameters in synthesis pathways for different PdRu nanoalloys.

| Reaction System | Metal Precursors | Reducing Agent | Ligand/Solvent | Temperature | Time | Product Morphology |
|---|---|---|---|---|---|---|
| PdRu NPs | $Pd(acac)_2$, $RuCl_3$ | $W(CO)_6$ | OAm + OA | 240°C | 40 min | Spherical Nanoparticles |
| PdRu NFs | $Pd(acac)_2$, $RuCl_3$ | $W(CO)_6$ | DMF | 120°C | 1 h | Flower-like assemblies of nanosheets |
| PdRu NSs | $Pd(acac)_2$, $Ru_3(CO)_{12}$ | $Ru_3(CO)_{12}$ (self-decomposition provides CO) | OAm | 180°C | 6 h | Hexagonal Nanosheets |

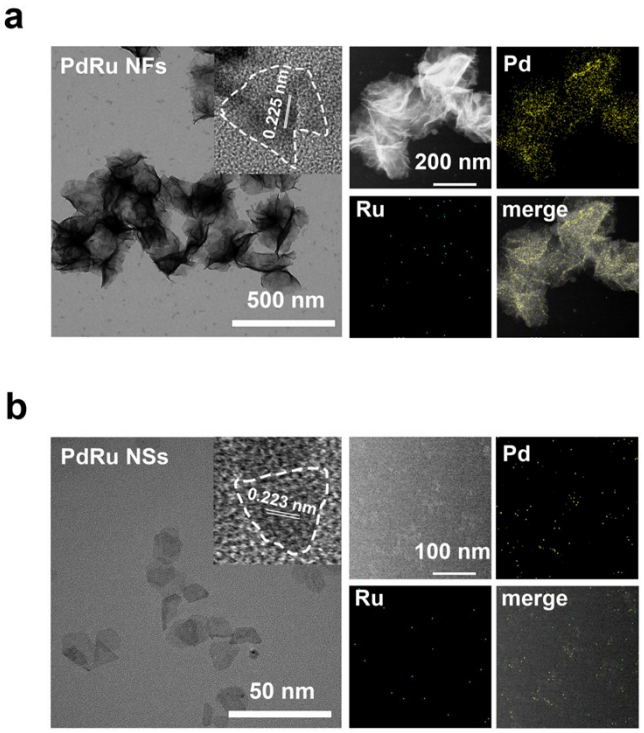


**Fig. S1.** TEM images, high-resolution TEM images (inset), high-angle annular dark-field scanning TEM images, and corresponding elemental mapping of (a) PdRu NFs and (b) PdRu NSs.

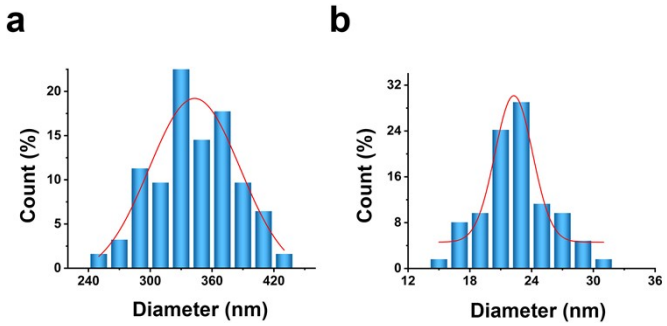


**Fig. S2.** Size distribution histogram of (a) PdRu NFs and (b) PdRu NSs.

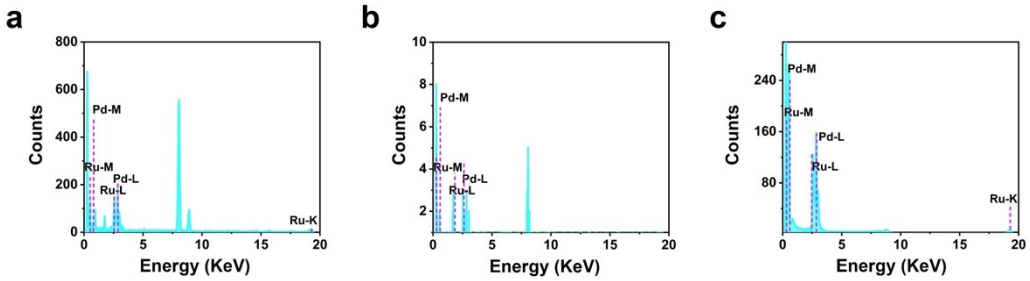


**Fig. S3.** The EDS spectra of (a) PdRu NPs, (b) PdRu NFs, and (c) PdRu NSs.

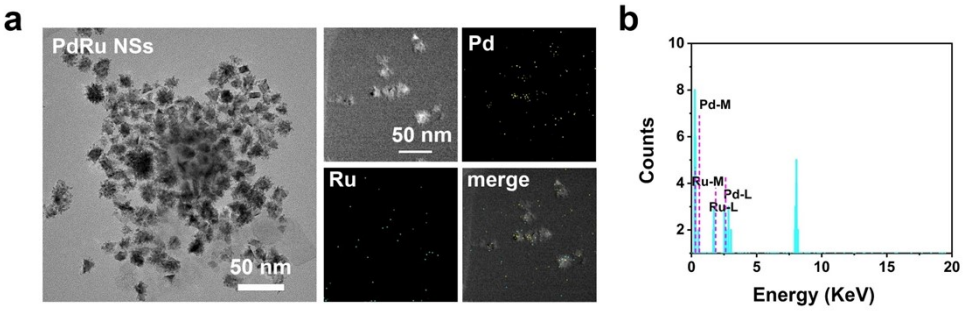


**Fig. S4.** TEM images and corresponding elemental mapping of PdRu NPs after laser-irradiation.

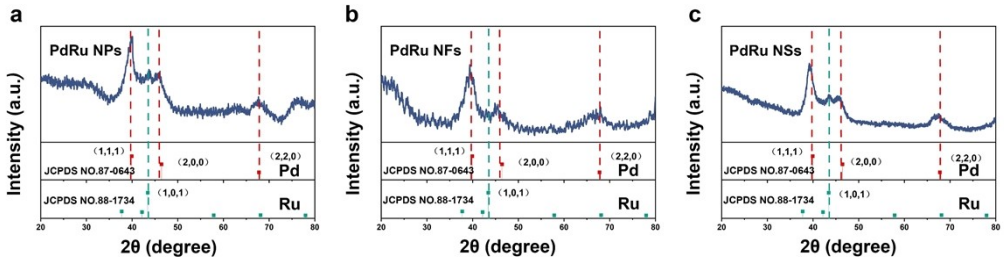


**Fig. S5.** XRD patterns of as-synthesized (a) PdRu NPs, (b) PdRu NFs, and (c) PdRu NSs.

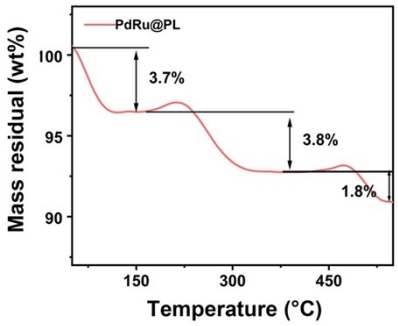


**Fig. S6.** The TGA curve of PdRu@PL**.**

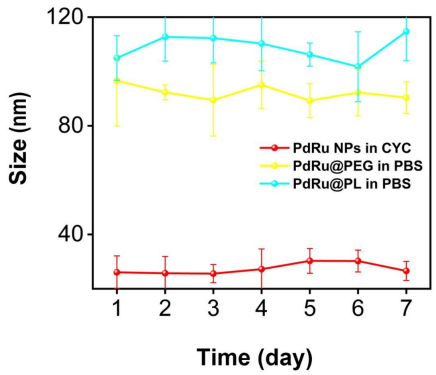


**Fig. S7.** Diameter of PdRu NPs in CYC, PdRu@PEG, and PdRu@PL in PBS over 7 days, as measured by DLS.

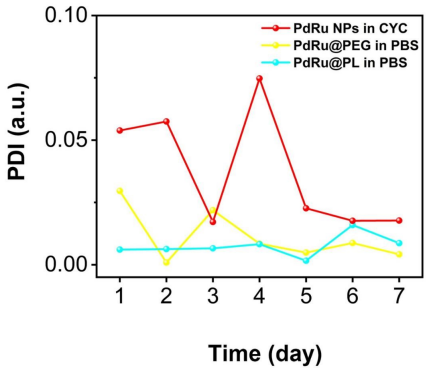


**Fig. S8.** Colloidal stability assessment monitored by absorbance over 7 days for PdRu NPs, PdRu@PEG, and PdRu@PL in their respective dispersion media.

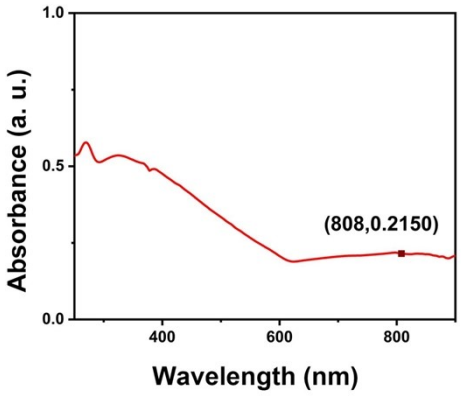


**Fig. S9.** Optical absorption spectrum of PdRu NPs.

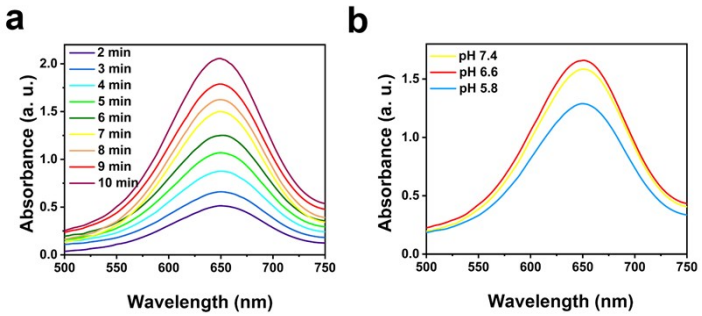


**Fig. S10.** UV−vis absorbance spectra of TMB for detection of ·OH at different (a) reaction times, and (b) pH.

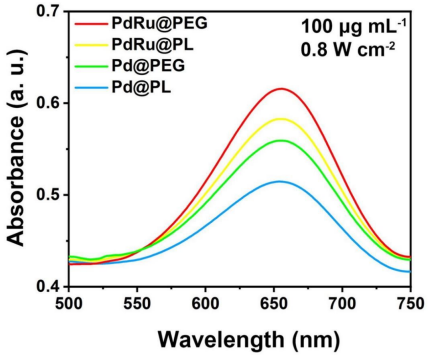


**Fig. S11.** UV−vis absorbance spectra of TMB for detection of ·OH at modified PdRu NPs and pure Pd NPs.

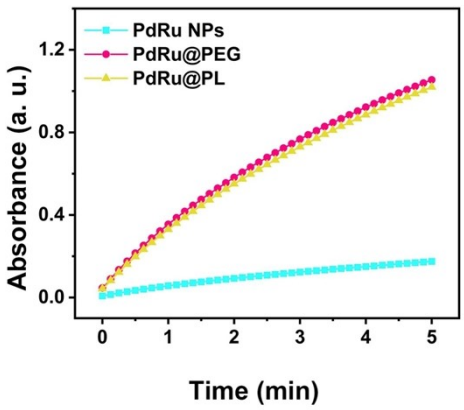


**Fig. S12.** The change of absorbance at 652 nm over time under the catalysis of PdRu NPs, PdRu@PEG, and PdRu@PL.

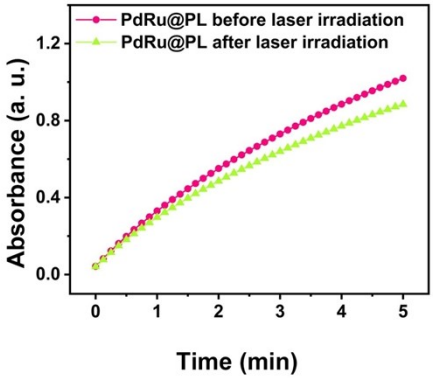


**Fig. S13.** The change of absorbance at 652 nm over time under the catalysis of PdRu@PL before/after laser irradiation.

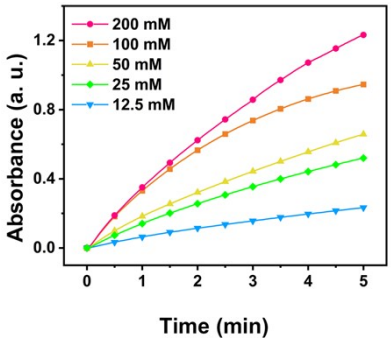


**Fig. S14.** The change of absorbance with time at 652 nm.

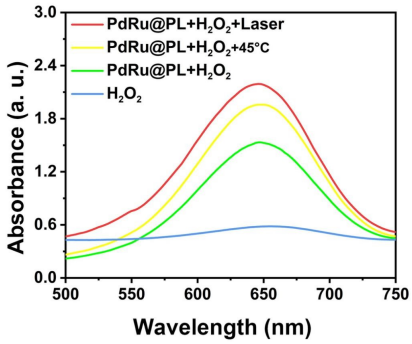


**Fig. S15.** UV−vis absorbance spectra of TMB for detection of ·OH at different conditions.

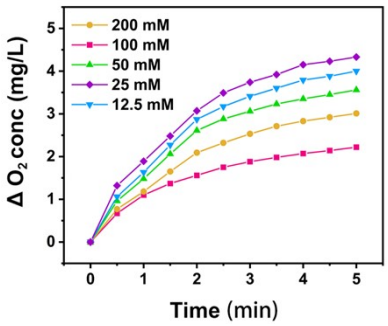


**Fig. S16.** Oxygen generation curves of PdRu@PL aqueous solutions with different concentrations of $H_2O_2$.

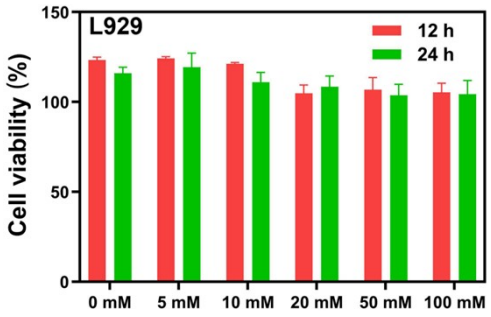


**Fig. S17.** Cell viabilities of PdRu@PL-treated L929 cells at different concentrations for 12 h and 24 h.

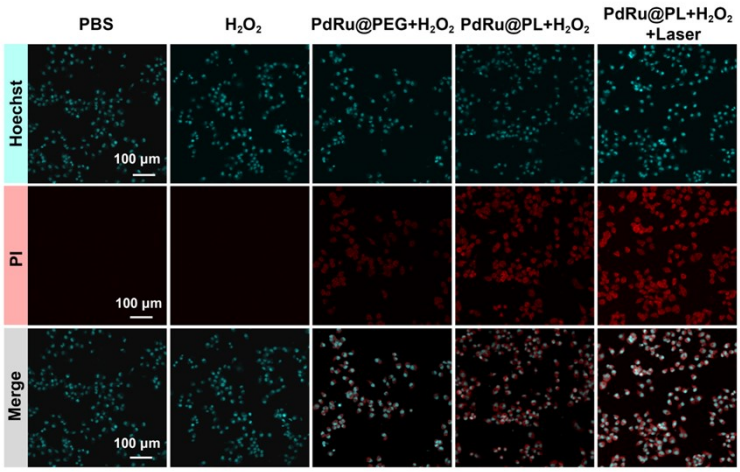


**Fig. S18.** Live/dead staining of the 4T1 cells with different treatments.

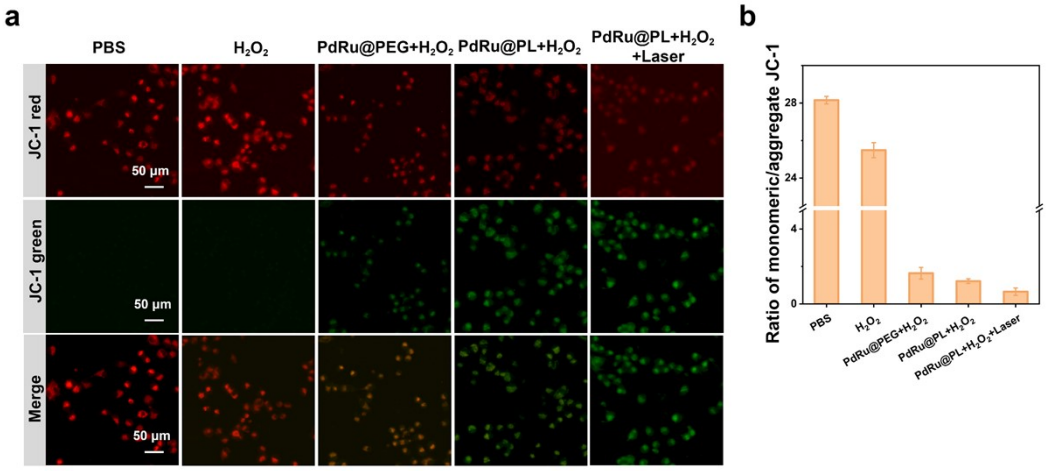


**Fig. S19.** (a)CLSM images, and (b) semi-quantitative analysis of mitochondria JC-1 staining treated with different conditions.

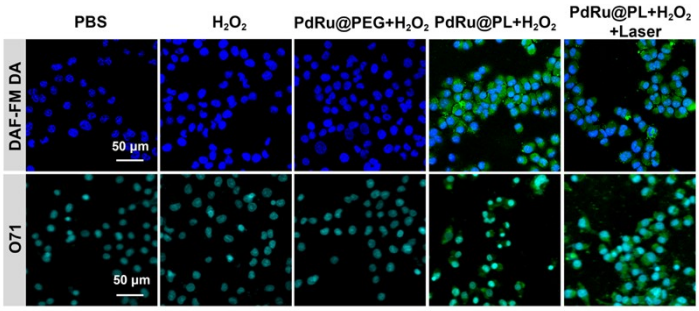


**Fig. S20.** Fluorescent images of 4T1 cells stained with DAF-FM DA and O71 after different treatments.

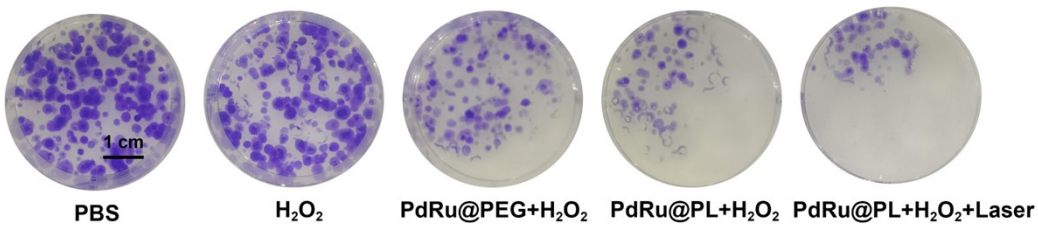


**Fig. S21.** Representative images of colony formation of 4T1 cells after different treatments.

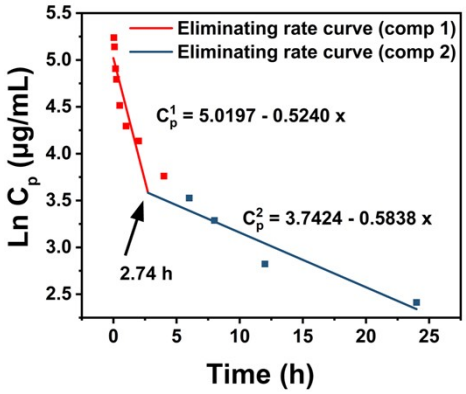


**Fig. S22.** The elimination rate curve of intravenously injected PdRu nanoalloys obtained from the blood circulation curve.

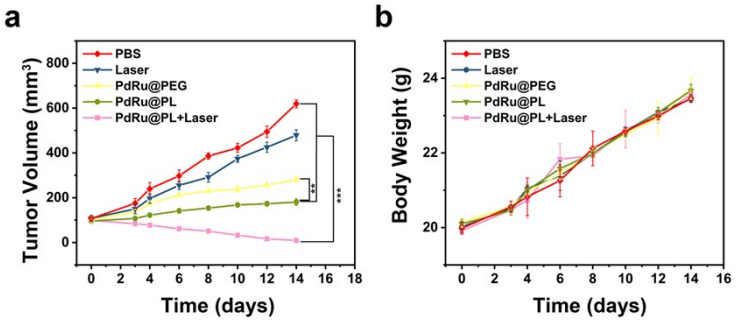


**Fig. S23.** (a)Tumor growth curves and (b) average body weight of mice after different treatments.

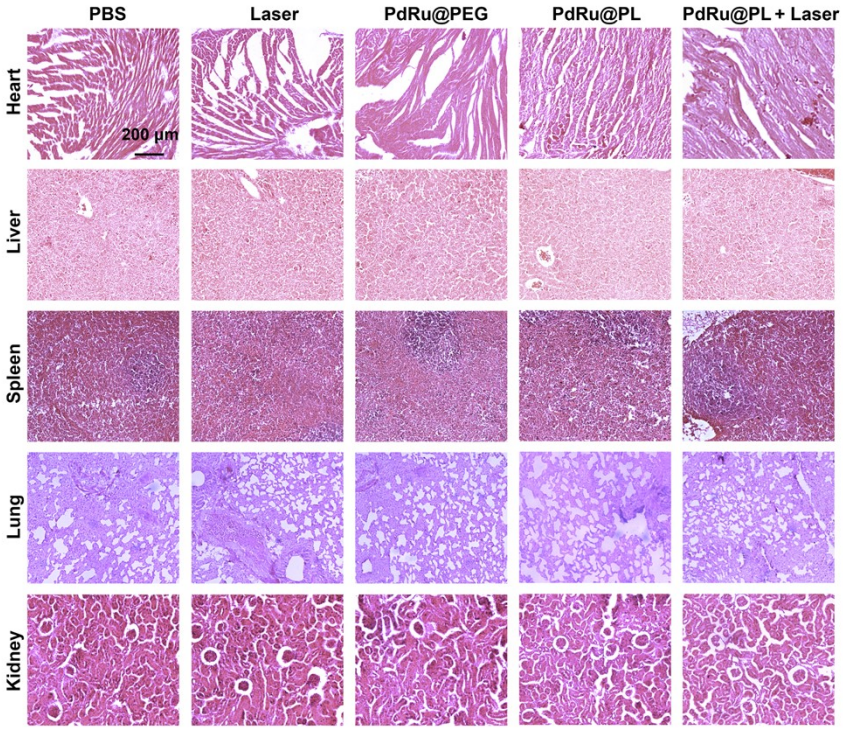


**Fig. S24.** Histological examination of major organs obtained from different groups after treatment.